SPECTROSCOPIC CONFIRMATION OF A $z = 2.79$ MULTIPLY IMAGED LUMINOUS INFRARED GALAXY BEHIND THE BULLET CLUSTER

Anthony H. Gonzalez[1], Casey Papovich[2], Maruša Bradač[3], and Christine Jones[4]

[1] Department of Astronomy, University of Florida, Gainesville, FL 32611-2055, USA; anthony@astro.ufl.edu
[2] Department of Physics, Texas A&M University, College Station, TX 77843-4242, USA
[3] Department of Physics, University of California at Davis, One Shields Avenue, Davis, CA 95616, USA
[4] Harvard-Smithsonian Center for Astrophysics, 60 Garden Street, Cambridge, MA 02138, USA

ABSTRACT

We report spectroscopic confirmation and high-resolution infrared imaging of a $z = 2.79$ triply imaged galaxy behind the Bullet Cluster. This source, a *Spitzer*-selected luminous infrared galaxy, is confirmed via polycyclic aromatic hydrocarbon (PAH) features using the *Spitzer* Infrared Spectrograph (IRS) and resolved with *Hubble Space Telescope* Wide Field Camera 3 imaging. In this galaxy, which with a stellar mass $M_* \approx 4 \times 10^9 \, M_\odot$ is one of the two least massive ones studied with IRS at $z > 2$, we also detect H_2 $S(4)$ and H_2 $S(5)$ pure rotational lines (at 3.1σ and 2.1σ)—the first detection of these molecular hydrogen lines in a high-redshift galaxy. From the molecular hydrogen lines we infer an excitation temperature $T = 377^{+68}_{-84}$ K. The detection of these lines indicates that the warm molecular gas mass is $6^{+36}_{-4}\%$ of the stellar mass and implies the likely existence of a substantial reservoir of cold molecular gas in the galaxy. Future spectral observations at longer wavelengths with facilities such as the *Herschel Space Observatory*, the Large Millimeter Telescope, and the Atacama Pathfinder Experiment thus hold the promise of precisely determining the total molecular gas mass. Given the redshift, and using refined astrometric positions from the high-resolution imaging, we also update the magnification estimate and derived fundamental physical properties of this system. The previously published values for L_{IR}, star formation rate, and dust temperature are confirmed modulo the revised magnification; however, we find that PAH emission is roughly a factor of 5 stronger than would be predicted by the relations between L_{IR} and L_{PAH} reported for SMGs and starbursts in Pope et al.

Key words: galaxies: evolution – galaxies: high-redshift – galaxies: starburst – gravitational lensing: strong

Online-only material: color figures

1. INTRODUCTION

An important legacy of the *Spitzer Space Telescope* is that it enabled the first detection of dust emission from a large number of luminous infrared galaxies at $z > 2$ (e.g., Papovich et al. 2006; Pérez-González et al. 2005), demonstrating that these galaxies dominate the massive galaxy population at high redshift. The implication is that at $z \sim 2$–3 massive galaxies are rapidly assembling their stars and growing supermassive black holes. For the most infrared-luminous systems, spectra from the *Spitzer* Infrared Spectrograph (IRS) have provided important insights into the physical processes driving L_{IR} (e.g., Houck et al. 2005; Yan et al. 2007). Pope et al. (2008) used IRS to demonstrate that the mid-IR properties of ultraluminous infrared galaxies (ULIRGs, $L_{IR} > 10^{12} \, L_\odot$) and submillimeter galaxies (SMGs) are distinct, with star-formation dominating the infrared emission for typical SMGs. It has been postulated by this group and others that such differences indicate different evolutionary stages, as the dominant source of L_{IR} transitions from star formation to active galactic nucleus (AGN) emission.

Existing studies like Pope et al. (2008) clearly demonstrate that IRS spectroscopy provides a clean means of disentangling the AGN and star formation contributions. A limitation to such work though is that current samples only probe the bright end of the luminosity function at high redshift (Dey et al. 2008; Dye et al. 2008), and IRS observations are practical for only a small subset of the most luminous sources. Observations of luminous infrared galaxies (LIRGS, $10^{11} \, L_\odot < L_{IR} < 10^{12} \, L_\odot$), the dominant class of IR galaxies at these redshifts

(Caputi et al. 2007, $\sim 10\times$ higher density than ULIRGS), have simply not been feasible. Gravitational lensing provides a means of circumventing this limitation, however, and several recent programs exploit strong lensing to study the properties of lensed galaxies at mid-IR and submillimeter wavelengths (Knudsen et al. 2008; Rigby et al. 2008, and references therein).

In this paper, we utilize a similar strategy to study a highly magnified LIRG that lies behind the Bullet Cluster (Markevitch et al. 2002). First identified in *Spitzer* IRAC imaging (Bradač et al. 2006), this galaxy has been shown to be a triply imaged optical drop-out (Gonzalez et al. 2009, hereafter Paper I) that is extremely luminous at submillimeter wavelengths (~ 0.11 Jy at $500 \, \mu$m; Wilson et al. 2008; Rex et al. 2009, 2010; Johansson et al. 2010). Photometric redshift estimates based upon both the stellar SED and the submillimeter emission place the galaxy at $z \sim 2.7$–2.9 (Wilson et al. 2008; Gonzalez et al. 2009; Rex et al. 2009), while lensing constraints imply magnification factors of 10–50 for each of the three images (Paper I). This galaxy therefore presents a unique opportunity to study in detail the properties of a member of the LIRG population during the peak epoch of star formation and galaxy assembly when these galaxies may be responsible for more than half the total infrared emission (Rodighiero et al. 2010).

We present in this paper the results of targeted observations of this lensed galaxy with *Spitzer* IRS spectroscopy and *Hubble Space Telescope* (*HST*) Wide Field Camera 3 (WFC3) infrared imaging. We combine these observations with both refined positions from the WFC3 imaging and published results from Wilson et al. (2008), Paper I, and Rex et al. (2009) to derive
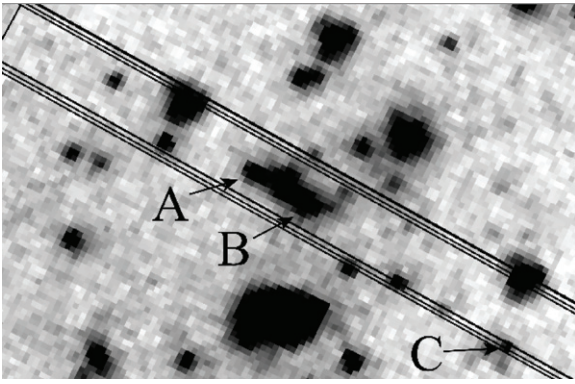
Figure 1. Shown here are the dithered IRS slit positions overlaid on the 8 μm image of the region. The three images of the LIRG are indicated with arrows and labeled A, B, and C. With this slit location we recover the combined spectrum of images A and B, but are not able to recover a spectrum for image C. Note that there is an elliptical galaxy that lies directly between images A and B in the 8 μm image. By 24 μm this elliptical contributes negligible flux in comparison to the two images of the LIRG (Paper I). The field of view is $65'' \times 50''$. North is up and east is to the left.

updated physical parameters for this galaxy. We also constrain the total contribution of a central AGN to the total mid-infrared emission. The data are presented in Section 2, while the analysis and derived physical properties are presented in Section 3. We summarize our results in Section 4. Throughout the paper we assume $H_0 = 70$ km s^{-1}, $\Omega_M = 0.27$, and $\Omega_\Lambda = 0.73$, consistent with the 5 year *Wilkinson Microwave Anisotropy Probe* cosmological analysis (Komatsu et al. 2009).

2. DATA

2.1. Spitzer IRS

We observed the galaxy on 2009 April 14–15 (PI: Gonzalez, program ID 496) using the Infrared Spectrograph (Houck et al. 2004) on board *Spitzer* during a single *Spitzer* Astronomical Observation Request to minimize alignment uncertainty. We targeted the source using the IRS LL1 module, which provides a spectrum in the wavelength interval 19–38 μm. This module was selected based upon the existing photometric redshifts, which indicated that the prominent polycyclic aromatic hydrocarbon (PAH) emission features should lie in this wavelength interval.

We centered the long slit on image B of the galaxy (see Figure 1). We used high-accuracy peak-up centroiding of stars from the Two Micron All Sky Survey (Skrutskie et al. 1997) with the IRS red filter to minimize deviations from the absolute telescope pointing. We did not restrict the spacecraft orientation for our data in order to maximize the likelihood that our observations would be executed prior to the end of the *Spitzer* cryogenic mission. Fortuitously, the slit orientation for our observations, 240°.9 east of north, placed both images A and B of the source within the slit. Therefore, our IRS observation contains the combined flux from the two brightest images of the galaxy. We were unable to extract a spectrum for image C, which lay on the very edge of the slit (see Figure 1). We obtained our IRS observations in the mapping mode with four $20''$ steps along the IRS slit. The total exposure time for the LL1 spectroscopy is 4×3.6 ks, where each map position consisted of 30 cycles with 120 s ramp duration.

We reduced the IRS data using software provided by the Spitzer Science Center (SSC),[5] and custom scripts (see Papovich

et al. 2009) based on techniques discussed in Teplitz et al. (2007). We started with the S18.7.0 *Spitzer* IRS pipeline data, which produced basic calibrated data (BCD) files. The IRS/LL arrays accumulate latent charge during long exposures (Teplitz et al. 2007). We measured and subtracted this latent charge by fitting a first-order polynomial to the mean counts per BCD as a function of time.

We next identified and cleaned known bad and hot pixels using the SSC task IRSCLEAN[6] with the known warm-pixel mask for our IRS campaign. We also identified other "rogue" and "warm" pixels as those with abnormally high variance, and used IRSCLEAN to interpolate over these pixels.

We constructed a sky spectrum for the lensed galaxy at each of the four slit positions by combining the BCDs of the three other slit positions. To create the sky image, we took the median of the stack of each pixel after rejecting outliers using a sigma-clipping algorithm. We performed this process iteratively, masking out the location of the lensed galaxy during subsequent iterations (the lensed galaxy is the only source we identify in the two-dimensional (2D) spectrum). We then subtracted the sky frame from each BCD and co-added the BCDs at each slit position. As a last step, we re-ran IRSCLEAN on the combined images for each slit position to clean any remaining hot pixels. These steps produced four 2D spectroscopic images for the lensed galaxy, one at each of the four slit positions.

We extracted 1D spectra at each slit position using the *Spitzer*/IRS custom extraction (SPICE) software.[7] Following Teplitz et al. (2007) we used a narrower extraction window than the default to minimize the noise contribution from the background. We used a window that had a width of $\approx$3.5 pixels at 27 μm and scaled with the wavelength. We estimated an aperture correction for this narrower aperture by comparing the spectra extracted using both the narrow and optimal extraction regions for the standard star HD 163466 taken in the same campaign as our science data. However, because the IRS observations of this star were taken in the staring mode, and because our science target is likely extended along the IRS slit, this aperture correction is unlikely to be perfect. The total flux density of the IRS spectrum integrated with the MIPS 24 μm passband we derived is $S(24 \mu\text{m}) = 0.925$ mJy, only slightly lower than $S(24 \mu\text{m}) = 0.965 \pm 0.028$ mJy co-added from images A and B from photometry in the MIPS 24 μm data in Paper I. Therefore the aperture correction we applied seems valid. Nevertheless, we multiplied the IRS spectrum by a factor of 1.04 to normalize to the MIPS data, thereby accounting for any remaining aperture effects and flux calibration issues. As noted in Paper I, the spectral energy distributions of the cluster elliptical and star that lie near the galaxy fall rapidly with wavelength and contribute negligibly at 24 μm. We therefore require no correction for these sources in the IRS spectral extraction.

To evaluate the errors in our spectra, we also extracted a sky spectrum using the same SPICE parameters at each slit position offset from the lensed galaxy. We use these sky spectra to estimate the error derived from the science spectra. Our tests showed that the errors derived from the sky were consistent with those propagated directly through the data reduction, and we use the latter in subsequent analyses. We then combined the four 1D spectra as a weighted mean, using the weights derived from the error spectra. The estimate of the variance on the combined science spectrum is the inverse sum of the weights. Figure 2 shows the resultant 1D science spectrum.
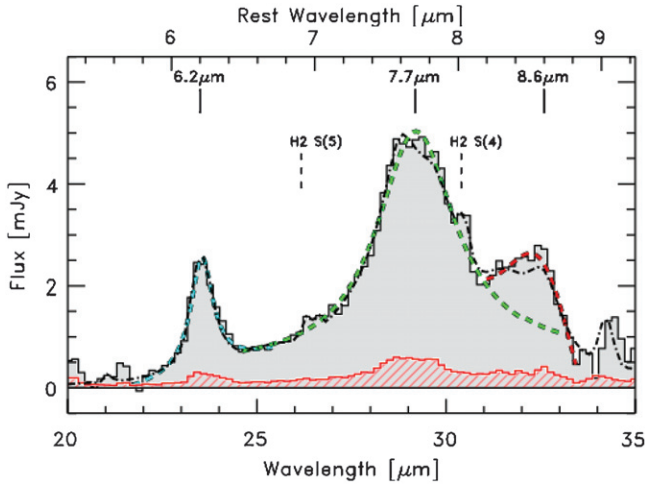
Figure 2. IRS spectrum of the galaxy, taken in the long-low mode. The data are presented as the shaded histogram, with the uncertainties shown by the hashed histogram. The dot-dashed line indicates the best fit from PAHFIT, while the dashed curves correspond to fits to the individual PAH lines using Drude profiles and the formulae from Smith et al. (2007). The vertical marks above the spectrum denote all spectral features robustly detected in our analysis.

(A color version of this figure is available in the online journal.)

2.2. HST Imaging

We obtained imaging with the *HST* Wide Field Camera 3 (Kimble et al. 2008) on 2009 November 19 and 20 (Cycle 17, proposal 11099, PI: Bradač), and with the Advanced Camera for Surveys (ACS; Ford et al. 2003) on 2006 October 12 and 13 (Cycle 15, proposal 10863, PI: Gonzalez) and 2004 October 21 (Cycle 13, proposal 10200, PI: Jones). The new WFC3 data consist of two overlapping WFC3/IR pointings in *F110W* and *F160W*, with total integration times at the location of the lensed LIRG (where the WFC3 pointings overlap) of 13 ks and 14 ks, respectively. The ACS data, which are described in Paper I, include *F606W*, *F775W*, and *F850LP* imaging.

All images were processed using standard calibration files and stacked using custom software from the HAGGLeS project (P. J. Marshall et al. 2010, in preparation) that is based upon MultiDrizzle (Koekemoer et al. 2002). To register the *F850LP*, *F110W*, and *F160W* images with the astrometric accuracy needed for this analysis (in particular since the standard distortion model we used did not give sufficient accuracy to simply align overlapping pointings), we determine the offsets among the images by extracting high signal-to-noise (S/N) objects in the individual, distortion corrected exposures. We use SExtractor (Bertin & Arnouts 1996) and the IRAF routine geomap to identify the objects and calculate the residual shifts and rotation of individual exposures, which were then fed back into Multidrizzle. We use *square* as the final drizzling kernel and an output pixel scale of 0″.1; this is smaller than the original pixel scale of the WFC3/IR, but larger than ACS CCD, allowing us to exploit the dithering of the observations and improve the sampling of the point-spread function.

3. ANALYSIS AND RESULTS

3.1. PAH Features and Redshift

The IRS spectrum for the galaxy is presented in Figure 2. The 6.2 μm, 7.7 μm, and 8.6 μm PAH complexes are detected in the spectrum. We also tentatively detect the H_2 0–0 $S(4)$ line, which is discussed separately in Section 3.8. We use Drude profiles, as in Smith et al. (2007), to model each spectral feature and

Table 1
Observed Fluxes and Magnitudes[a]

Quantity	Value
$f(6.2\,\mu m)$	$1.4 \pm 0.2 \times 10^{-14}$ erg s^{-1} cm^{-2}
$f(7.7\,\mu m)$	$6.3 \pm 1.2 \times 10^{-14}$ erg s^{-1} cm^{-2}
$f(8.6\,\mu m)$	$5.2 \pm 3.3 \times 10^{-14}$ erg s^{-1} cm^{-2}
$f(H_2 S(4))$	$5.8 \pm 1.9 \times 10^{-15}$ erg s^{-1} cm^{-2}
$f(H_2 S(5))$	$2.5 \pm 1.2 \times 10^{-15}$ erg s^{-1} cm^{-2}
$f(7.7\,\mu m)/f(6.2\,\mu m)$	4.5 ± 1.1
m_{F160W}	23.80 ± 0.1 (AB)

Note. [a] All quoted values are for the combination of images A and B.

use a power law to fit the underlying continuum. We derive the redshift from the two strongest PAH features (6.2 μm and 7.7 μm), obtaining $z = 2.791 \pm 0.007$. This redshift confirms the photometric redshifts in the literature ($z \sim 2.7$–2.9; Wilson et al. 2008; Gonzalez et al. 2009; Rex et al. 2009).

The derived fluxes for the PAH features are listed in Table 1. The flux ratio for the two highest S/N lines, $f(7.7\,\mu m)/f(6.2\,\mu m) = 4.5 \pm 1.1$, can be compared with results from Pope et al. (2008) for SMGs. The star formation dominated SMGs in the Pope et al. sample ($z \sim 1$–2.5) have flux ratios in the range of 1.4–3.5 for these PAH lines—somewhat lower than the ratio we observe, but with a range that overlaps the 1σ uncertainty for this galaxy.

3.2. WFC3 Imaging of the Lensed Galaxy

With the new *HST* WFC3 imaging we repeat the photometric analysis described in Paper I to try to identify the lensed galaxy in high-resolution photometry. We show in Figure 3 (left panel) a composite color image constructed from the *F850LP*, *F110W*, and *F160W* images. The lensed galaxy can be seen in the composite image as a faint red arc that contains brighter knots of emission in the vicinity of images A and B from the *Spitzer* data.

We use *GALFIT* version 3.0 to model and subtract foreground objects near the location of the lensed galaxy. The object, which is not detected in *F850LP* (Paper I), is detected in *F110W* but is too faint relative to the model residuals to recover robust photometry. The arc is bright, however, in *F160W* (Figure 3, right panel). To verify that this arc is indeed the same lensed galaxy as identified at longer wavelengths, we measure the flux ratio for the two lobes of the arc. Specifically, we extract the fluxes within polygonal apertures enclosing each of the bright emission regions and correct for the sky using background apertures placed on nearby blank sky regions. We measure a flux ratio $B/A = 1.4 \pm 0.3$—consistent with results at longer wavelengths in Paper I (see also Section 3.3). The total magnitude for the entire arc (images A and B) is $m_{F160W} = 23.80 \pm 0.1$ (AB), which corresponds to a flux density of $1.1 \pm 0.1\,\mu$Jy. As shall become clear in Section 3.3, without magnification this object would be extremely faint, with $m_{F160W} \approx 28.8$. We refrain from quoting a flux density at *F110W* due to the lower contrast with the foreground galaxy and higher associated systematic uncertainties.

3.3. Magnification

Conversion of the PAH line fluxes to luminosities requires not only the redshift but also a determination of the lensing magnification. We use the same mass maps described in Paper I. Consequently, the only changes from the previous analysis are
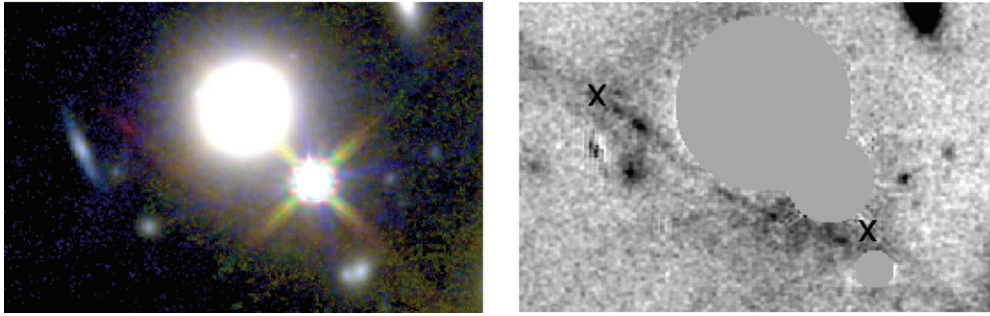
Figure 3. *HST* imaging of a $14'' \times 9''$ region encompassing the lensed galaxy. The image on the left is a color composite using the *F850LP*, *F110W*, and *F160W* bands for blue, green, and red, respectively. Despite the bright foreground galaxy, the lensed galaxy can be seen as a red arc with two lobes. On the right, we show the *F160W* image of the same region after the bright foreground objects have been modeled with GALFIT and subtracted. In this image, we also mask the cores of the three brightest objects for clarity. The arc, which is clearly visible in this image, breaks up into two lobes corresponding to images A and B in the IRAC imaging from Paper I. Crosses denote the positions previously reported based upon IRAC photometry. The offsets are consistent with the uncertainties in the IRAC positions due to source blending. North is up and east is to the left.

(A color version of this figure is available in the online journal.)

the spectroscopic redshift and improved astrometric positions. The former has only a modest impact, whereas the latter have a more significant impact because of the steep magnification gradient near the critical curve.

In the current discussion, we are concerned primarily with images A and B. The WFC3 astrometry moves both images A and B slightly closer to the critical curve and consequently raises the derived magnifications. At the location of image A we compute a magnification $|\mu_A| \sim 32$ and at image B we obtain $|\mu_B| \sim 69$. The measured flux ratio of the two images from Paper I is 1.47 ± 0.05. To estimate the range of plausible magnification for the blended IRS spectrum, we take individually the predicted magnifications for A and B at the locations of peak emission for each arc and combine these with the observed flux ratio.[8] We find that the total combined magnification is $|\mu_{AB}| \sim 80$–115. In subsequent discussions, we will quote quantities in terms of $\mu_{AB}/100$ to reflect the intrinsic uncertainty in the magnification. In Paper I, we used $\mu_A/25$, which corresponds to $\mu_{AB} = 80$.

3.4. Presence of an AGN

In Paper I, we considered the question of whether the infrared emission in this object is driven by star formation or AGN activity. Based upon the hint of spatial extension in the IRAC data and lack of X-ray detection, we argued that the emission cannot be purely due to an AGN. We further concluded that the observed mid-infrared colors (4.5 to 24 μm) indicated that the source spectral energy distribution may be a composite with contributions from both starburst and AGN contributions.

We now revisit this question based upon both the IRS spectroscopy and WFC3 imaging. From the spectral analysis we can also place an upper bound on the contribution of the AGN to the mid-infrared emission by estimating the fraction of the flux contained in the power-law continuum. From the 5.7 to 8.8 μm rest frame, the continuum contributes ~45% of the total emission, confirming that the AGN is not dominant at mid-infrared wavelengths, but leaving the possibility that it may be a significant contributor to the far-infrared emission.

Additional information is provided by the WFC3 imaging, in which we resolve the target galaxy into gravitational arcs. As discussed in Section 3.2, the flux ratio for components A and

B in the *F160W* observations is consistent with the 24 μm flux ratio. Because we are probing near the critical curves where there are strong magnification gradients, this should not necessarily be the case unless the stellar emission and PAH emission have similar spatial distributions within the galaxy. Thus, the WFC3 data further support the picture that in this galaxy the mid- and far-infrared emission is dominated by star formation.

3.5. Stellar Population Age and Mass

We present in Figure 4 the full spectral energy distribution for the combination of images A and B, including all published data. Given the redshift, we can now repeat the analyses of the SED presented in Paper I to refine the physical constraints on the system.

We first use HyperZ (Bolzonella et al. 2000) to derive improved constraints on the age of the dominant stellar population and total internal absorption of the system. As in Paper I, the input spectral templates are based upon the 2007 Charlot & Bruzual models with the Padova 1994 evolutionary tracks (Bertelli et al. 1994) and a Chabrier (2003) mass function. We use a Calzetti et al. (2000) extinction law to estimate the internal extinction, and fit the photometry at observed wavelengths $\lambda < 10\,\mu$m to exclude PAH emission. We refer the reader to Paper I for further details. In deriving confidence intervals on the age and extinction, we find that the data are best fit by a 10 Myr population. The solutions for the emission-weighted age bifurcate though, permitting both very young templates and solutions with ages of a few Gyr. The 90% confidence intervals on the age are $t < 90$ Myr and 1.4 Gyr $< t < 2.6$ Gyr. We note however that strong observed submillimeter emission provides a compelling argument for a very young stellar population. The extinction meanwhile is constrained to be $A_V = 3.8^{+0.5}_{-1.0}$ (90% confidence). The confidence interval reduces to $A_V = 3.8^{+0.5}_{-0.2}$ if one considers only the younger age solutions.

Next, we update our estimate of the stellar mass using the code kcorrect (Blanton & Roweis 2007), as in Paper I. We fit the combined flux from images A and B, using the data at observed wavelengths of 1.5–8 μm. For $z = 2.79$ and $A_V = 3.8$, we obtain a stellar mass $M_* = 4 \times 10^9 (\mu_{AB}/100)^{-1} M_\odot$.[9] This value is roughly a factor of 3 lower than the previously published

---

[8] Our magnification maps do not have the accuracy to resolve structure on the scale of the arcs, so we do use this point estimate rather than averaging over the photometric apertures.

[9] An important caveat to keep in mind is that systematic uncertainties in stellar mass estimates can yield a factor of 2 or greater errors (Conroy et al. 2009).
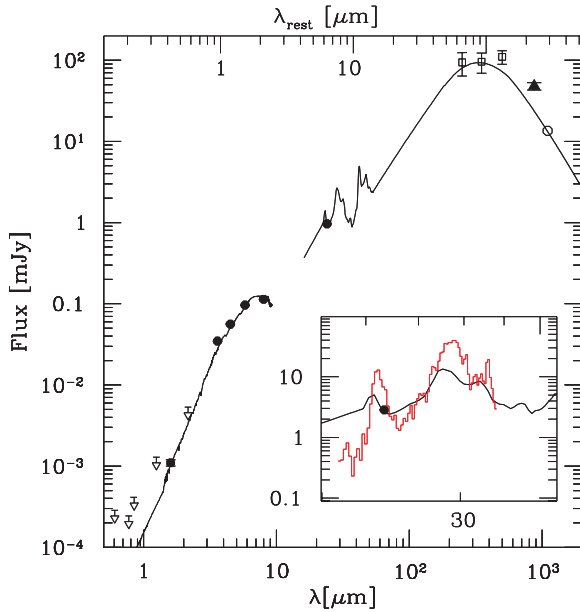
Figure 4. Spectral energy distribution for the combination of images A and B (i.e., total flux density in A+B), including data points from Wilson et al. (2008, open circle), Paper I, Rex et al. (2009, open squares), and Johansson et al. (2010, solid triangle) in addition to the photometry and spectra presented in this paper. All downward pointing open arrows are upper limits. The solid lines correspond to the best-fit models from HyperZ and the Chary & Elbaz (2001) templates. The inset shows the model compared with the IRS spectrum (histogram) and $24\,\mu$m data point.

(A color version of this figure is available in the online journal.)

result. The added leverage from the $1.6\,\mu$m data point is the largest factor in the decrease, with the addition of this data point accounting for roughly a factor of 2. The revised magnification estimates account for the remainder of the change, while the changes in redshift and extinction have only a minor impact. The updated stellar mass implies that the target is a low-mass dwarf galaxy.

3.6. Total Infrared Luminosity

There exist multiple different techniques for estimating the total infrared luminosity for a galaxy where the infrared emission is dominated by star formation. The preferred technique is to use data spanning the peak of the far-infrared (FIR) spectral energy distribution and directly fit a modified blackbody to the far-infrared emission. This technique, which should now become the default method in the era of *Herschel*, provides the most straightforward constraint on $L_{\rm IR}$ with the added advantage of directly yielding the temperature of the dust if the redshift is known. Many past studies, in the absence of the requisite FIR data, have instead utilized either $24\,\mu$m emission or PAH luminosities to estimate $L_{\rm IR}$. With the unique data sets available for our lensed galaxy behind the Bullet Cluster, we are able to compare estimates via all three approaches and assess the level of consistency for this particular dusty starburst.

We first consider the direct approach. Rex et al. (2009) previously reported $L_{\rm IR} = 2 \times 10^{11} (\mu_{AB}/100)^{-1} L_\odot$ and a dust temperature $T \sim 32$ K for this system using data from AzTEC and BLAST with an assumed redshift of $z = 2.9$. Johansson et al. (2010) recently reported an $870\,\mu$m flux density from the Large APEX BOlometer CAmera (LABOCA) and noted that the 1.1 mm data point from Wilson et al. (2008) will soon be revised upward to $\sim$20 mJy. The primary impact will be a $\sim$10% revision in the dust temperature and $L_{\rm IR}$, which are both within

the presumed uncertainties. The *Herschel* Lensing Survey (PI: Egami) should soon significantly improve determinations of both quantities (see Rex et al. 2010).

Second, we estimate $L_{\rm IR}$ using the $24\,\mu$m emission alone, without separating the PAH from continuum emission. This method is predicated on matching the observed $24\,\mu$m luminosity to a best-fit spectral energy distribution. As in Paper I we use the code and templates from Chary & Elbaz (2001) to calculate the bolometric infrared luminosity. Updating the magnification and redshift from the previous analysis, we obtain $L_{\rm IR} = 3 \pm 0.3 \times 10^{11} (\mu_{AB}/100)^{-1} L_\odot$. This value is broadly consistent with the modified blackbody fit to $24\,\mu$m–1 mm data, predicting well the shorter wavelength BLAST data points and the published AzTEC 1.1 mm result. The disagreement with the longer wavelength data points and expected upward revision to the AzTEC data can be considered a possible indication of a cooler dust temperature than in the Chary & Elbaz (2001) templates.[10]

Finally, we consider the observed emission from the PAH features, which are known to be strongly correlated with star formation. Pope et al. (2008) presented PAH luminosities for a sample of 13 SMGs (predominantly ultraluminous infrared galaxies with $L_{\rm IR} > 2 \times 10^{12}$) at $z = 0.9$–2.3. Combining these with total infrared luminosities from Pope et al. (2006), and including a sample of lower luminosity low-redshift starburst galaxies, the authors derived a relation between PAH and total infrared luminosity for star formation dominated infrared galaxies.

For the magnification derived in Section 3.3, we find that the observed PAH features have luminosities $L(6.2\,\mu{\rm m}) = 2.4 \pm 0.4 \times 10^9 (\mu_{AB}/100)^{-1} L_\odot$ and $L(7.7\,\mu{\rm m}) = 1.1 \pm 0.2 \times 10^{10} (\mu_{AB}/100)^{-1} L_\odot$. Following the Pope et al. (2008) relations, we compute that $L_{\rm IR} = 9.3 \pm 1.6 \times 10^{11} (\mu_{AB}/100)^{-1} L_\odot$ and $L_{\rm IR} = 1.46 \pm 0.27 \times 10^{12} (\mu_{AB}/100)^{-1} L_\odot$ from the $6.2\,\mu$m and $7.7\,\mu$m lines, respectively. The quoted errors include the uncertainties in the PAH measurements and in the coefficients of the Pope et al. (2008) $L_{\rm PAH}$–$L_{\rm IR}$ relations, but do not include intrinsic scatter in the $L_{\rm PAH}$–$L_{\rm IR}$ relations. The two PAH lines give values that are factors of 5–7 and 3–5 higher than the estimates based upon the FIR emission and $24\,\mu$m template fitting, respectively. This offset can plausibly be argued as being due to the intrinsic scatter about the mean relation since the few galaxies in this luminosity regime in Pope et al. (2008) also exhibit large scatter; however, similar offsets are also seen for the lensed SMG SMM J1643554.2+661225, MS1512-cB58, and the Cosmic Eye, which all have $10^{11}\,M_\odot < L_{\rm IR} < 10^{12}\,M_\odot$ (Papovich et al. 2009; Siana et al. 2009). Moreover, Rigby et al. (2008) observe a comparable enhancement in $L(8\,\mu{\rm m})/L_{\rm IR}$ for LIRGs at $z \sim 2$. Together these results argue for a possible systematic shift relative to the Pope et al. (2008) relation at LIRG luminosities.

3.7. Star Formation Rate

To estimate the star formation rate (SFR), we use the $L_{\rm IR}$ determinations based upon the FIR emission and $24\,\mu$m template fitting. Following the Kennicutt (1998) relation, these $L_{\rm IR}$ estimates imply SFR $\approx$ 100–150 $M_\odot$ yr^{-1}.

Combining these values with the revised stellar mass, the estimated specific star formation rate (SSFR) for this galaxy is

---

[10] A change in the normalization of the blackbody to match the BLAST and revised AzTEC data would yield a poor fit to the data near the peak; only a cooler dust temperature can simultaneously fit all the millimeter and submillimeter data.

SSFR ≈ 25–$40\,\mathrm{Gyr}^{-1}$. The SSFR and stellar mass are consistent with the results for low-mass BM/BX and Lyman break galaxies (LBGs) in Reddy et al. (2006). These results thus imply that this particular galaxy is not unique, but rather indicative of the general low-mass, star-forming population at this epoch.

3.8. Molecular Hydrogen

We detect the H_2 0–0 $S(4)$ pure rotational line at rest frame $8.025\,\mu m$ in the IRS spectrum, and also have a tentative (2σ) detection of the H_2 0–0 $S(5)$ line at $6.909\,\mu m$—the first detection of these lines in a high redshift galaxy. Fitting Drude profiles, we derive line fluxes of $f(H_2\ S(4)) = (5.8 \pm 1.9) \times 10^{-15}\,\mathrm{erg\,s^{-1}\,cm^{-2}}$ and $f(H_2\ S(5)) = (2.5 \pm 1.2) \times 10^{-15}\,\mathrm{erg\,s^{-1}} cm^{-2}$ (Table 1). These fluxes correspond to luminosities of $(4.0 \pm 1.3) \times 10^{42}\,(\mu_{AB}/100)^{-1}\,\mathrm{erg\,s^{-1}}$ and $(1.7 \pm 0.8) \times 10^{42}\,(\mu_{AB}/100)^{-1}\,\mathrm{erg\,s^{-1}}$, respectively. The $S(4)$ line strength is exceptionally strong, with a luminosity that exceeds that of the nearby LIRG NGC 6240 ($L_{IR} \sim 7 \times 10^{10}\,L_\odot$) by more than a factor of 50 (Armus et al. 2006).

The ratio of these two lines can be used to directly constrain the excitation temperature of the gas. Physically, for lower excitation temperatures a greater fraction of the gas is in the low energy states and the fraction of H_2 emitting in $S(4)$ decreases correspondingly. The observed ratio $f(H_2\ S(5))/f(H_2\ S(4)) = 0.42 \pm 0.24$ implies $T = 377^{+68}_{-85}$ K for a single temperature gas—relatively cool compared to systems with shocked gas (e.g., Armus et al. 2006; Egami et al. 2006). The corresponding constraint on the warm molecular gas mass can then be computed as

$$M_{H_2} = m_H N_{H_2}$$
$$= m_H \frac{N(v,i)}{g_i} \exp(E(v,j)/kT) \sum_{j=0}^{\infty} g_j \exp(-E(v,j)/kT), \tag{1}$$

where g_i are the statistical weights of the energy states (see Rosenthal et al. 2000) and the number density for the $S(4)$ transition can be calculated as

$$N(v,i) = \frac{L(v,i)}{A(v,i)h\nu_i}, \tag{2}$$

where $L(v,i)$ is the luminosity and $A(v,i)$ is the Einstein coefficient. From this approach we derive a warm molecular gas mass $M_{H_2} = 2.2^{+17}_{-0.8} \times 10^8\,(\mu_{AB}/100)^{-1}\,M_\odot$. This value serves as a lower bound on the total molecular gas content of this system since we do not presently probe the cold gas. Equivalently, this warm gas mass is $6^{+36}_{-4}\%$ of the stellar mass derived in Section 3.5. For comparison, in their study of the lensed LBG J213512.73−010143, Coppin et al. (2007) use CO data to derive a cold molecular gas mass of 2.4×10^9, which is 30% of the stellar mass—consistent with what we see in this system (albeit with large uncertainty).

The observed molecular emission is thus consistent with the picture of a relatively cool ($T \sim 375$ K) dusty starburst with a significant gas reservoir. A more detailed confirmation of this picture will require future observations of either the $S(1)$–$S(3)$ lines or CO rotational lines at longer wavelength, which will enable a robust determination of the total gas content. Finally, we note that the lensed LBGs J213512−01043 and MS1512-cB58 are the only galaxies with similar L_{IR} and redshift for which gas masses have been determined via the CO (3–2) line (Baker

Table 2
Summary Table of Derived Physical Properties

Quantity	Value
z	2.791 ± 0.007
$|\mu_{AB}|$	80–115
A_V[a]	$3.8^{+0.5}_{-1.0}$
Age[a,b]	< 90 Myr
SFR	100–$150\,M_\odot\,\mathrm{yr}^{-1}$
SSFR	25–$40\,\mathrm{Gyr}^{-1}$
M^*	$4 \times 10^9\,M_\odot$
M_{H_2}	$> 4 \times 10^8\,M_\odot$
T_{H_2}	275–375 K
L_{IR} (24 μm)	$3 \pm 0.3 \times 10^{11}\,L_\odot$
L_{IR} (FIR)[c]	$2 \times 10^{11}\,L_\odot$
L_{IR} (PAH,6.2 μm)	$9.3 \pm 1.6 \times 10^{11}\,L_\odot$
L_{IR} (PAH,7.7 μm)	$1.46 \pm 0.27 \times 10^{12}\,L_\odot$

Notes.
[a] Confidence interval is 90% rather than 1σ.
[b] All quantities listed after age presume $\mu_{AB} = 100$.
[c] Value from Rex et al. (2009).

et al. 2004; Coppin et al. 2007).[11] The lensed galaxy described in this paper exhibits much greater extinction and thus provides complementary information.

4. SUMMARY AND DISCUSSION

In this paper, we present IRS spectroscopic confirmation of a luminous infrared galaxy at $z = 2.79$ that is highly magnified by the Bullet Cluster. We also spatially resolve the galaxy with WFC3, revealing gravitational arcs near the previously determined *Spitzer* positions. The redshift determination and high S/N of the spectrum, coupled with the multiwavelength photometry, enable us to refine our previous analysis of the physical properties of this galaxy. We determine that the lensed object is a low-mass dwarf galaxy, $M_* = 4 \times 10^9\,(\mu_{AB}/100)^{-1}\,M_\odot$, for which the far-infrared thermal emission is star formation dominated. The inferred SSFR ≈ 25–$40\,\mathrm{Gyr}^{-1}$ is typical for a field galaxy of this mass at this redshift (e.g., Reddy et al. 2006). The observed and derived physical quantities are summarized in Tables 1 and 2.

By virtue of the extreme lensing—the two brightest images have a combined magnification of roughly 100—this object thus provides a powerful laboratory in which to probe the conditions in low-mass, star-forming galaxies during an epoch when they are otherwise inaccessible. Indeed, this galaxy is one of the two lowest mass systems with IRS spectroscopy at $z > 2$.[12] Perhaps most promising for future investigations, our detection of rotational H_2 lines is indicative of a large molecular gas reservoir. We derive a temperature of $T = 377^{+68}_{-85}$ K and estimate a gas mass of $M_{H_2} = 2.2^{+17}_{-0.8} \times 10^8\,M_\odot$ in this component, roughly 2%–42% of the stellar mass. Future spectroscopic observations of longer wavelength H_2 lines with *Herschel* and CO rotational lines with a facility such as the Large Millimeter Telescope or the Atacama Pathfinder EXperiment (APEX) therefore have the potential to precisely measure the total molecular gas content in this galaxy. Finally, we note that because dwarf galaxies of this mass are a ubiquitous population, the odds are good that programs like the *Herschel* Lensing

---

[11] The SMG SMM J2135−0102, which has a factor of ~ 4 higher L_{IR}, also has a gas mass via the CO (1–0) line (Swinbank et al. 2010).
[12] The lensed LBG MS1512-cB58 has a factor of ~ 2–4 lower stellar mass (see Siana et al. 2008).

Survey can detect a sizable sample of similar lensed sources behind massive clusters.

REFERENCES

Armus, L., et al. 2006, ApJ, 640, 204
Baker, A. J., Tacconi, L. J., Genzel, R., Lehnert, M. D., & Lutz, D. 2004, ApJ, 604, 125
Bertelli, G., Bressan, A., Chiosi, C., Fagotto, F., & Nasi, E. 1994, A&AS, 106, 275
Bertin, E., & Arnouts, S. 1996, A&AS, 117, 393
Blanton, M. R., & Roweis, S. 2007, AJ, 133, 734
Bolzonella, M., Miralles, J.-M., & Pelló, R. 2000, A&A, 363, 476
Bradač, M., et al. 2006, ApJ, 652, 937
Calzetti, D., Armus, L., Bohlin, R. C., Kinney, A. L., Koornneef, J., & Storchi-Bergmann, T. 2000, ApJ, 533, 682
Caputi, K. I., et al. 2007, ApJ, 660, 97
Chabrier, G. 2003, PASP, 115, 763
Chary, R., & Elbaz, D. 2001, ApJ, 556, 562
Conroy, C., Gunn, J. E., & White, M. 2009, ApJ, 699, 486
Coppin, K. E. K., et al. 2007, ApJ, 665, 936
Dey, A., et al. 2008, ApJ, 677, 943
Dye, S., et al. 2008, MNRAS, 388, 384
Egami, E., Rieke, G. H., Fadda, D., & Hines, D. C. 2006, ApJ, 652, L21
Ford, H. C., et al. 2003, Proc. SPIE, 4854, 81
Gonzalez, A. H., Clowe, D., Bradač, M., Zaritsky, D., Jones, C., & Markevitch, M. 2009, ApJ, 691, 525 (Paper I)
Houck, J. R., et al. 2004, Proc. SPIE, 5487, 62
Houck, J. R., et al. 2005, ApJ, 622, L105
Johansson, D., et al. 2010, A&A, 514, 77
Kennicutt, R. C., Jr. 1998, ApJ, 498, 541
Kimble, R. A., MacKenty, J. W., O'Connell, R. W., & Townsend, J. A. 2008, Proc., SPIE, 7010, 70101E
Knudsen, K. K., van der Werf, P. P., & Kneib, J.-P. 2008, MNRAS, 384, 1611
Koekemoer, A. M., Fruchter, A. S., Hook, R. N., & Hack, W. 2002, in The 2002 HST Calibration Workshop: Hubble after the Installation of the ACS and the NICMOS Cooling System, ed. S. Arribas, A. Koekemoer, & B. Whitmore (Baltimore: STScI), 337
Komatsu, E., et al. 2009, ApJS, 180, 330
Markevitch, M., Gonzalez, A. H., David, L., Vikhlinin, A., Murray, S., Forman, W., Jones, C., & Tucker, W. 2002, ApJ, 567, L27
Papovich, C., Rudnick, G., Rigby, J. R., Willmer, C. N. A., Smith, J., Finkelstein, S. L., Egami, E., & Rieke, M. 2009, ApJ, 704, 1506
Papovich, C., et al. 2006, ApJ, 640, 92
Pérez-González, P. G., et al. 2005, ApJ, 630, 82
Pope, A., et al. 2006, MNRAS, 370, 1185
Pope, A., et al. 2008, ApJ, 675, 1171
Reddy, N. A., Steidel, C. C., Fadda, D., Yan, L., Pettini, M., Shapley, A. E., Erb, D. K., & Adelberger, K. L. 2006, ApJ, 644, 792
Rex, M., et al. 2009, ApJ, 703, 348
Rex, M., et al. 2010, A&A, 518, 13
Rigby, J. R., et al. 2008, ApJ, 675, 262
Rodighiero, G., et al. 2010, A&A, 515, A8
Rosenthal, D., Bertoldi, F., & Drapatz, S. 2000, A&A, 356, 705
Siana, B., Teplitz, H. I., Chary, R., Colbert, J., & Frayer, D. T. 2008, ApJ, 689, 59
Siana, B., et al. 2009, ApJ, 698, 1273
Skrutskie, M. F., et al. 1997, in ASSL 210, The Impact of Large Scale Near-IR Sky Surveys, ed. F. Garzon et al. (Dordrecht: Kluwer), 25
Smith, J. D. T., et al. 2007, ApJ, 656, 770
Swinbank, A. M., et al. 2010, Nature, 464, 733
Teplitz, H. I., et al. 2007, ApJ, 659, 941
Wilson, G. W., et al. 2008, MNRAS, 390, 1061
Yan, L., et al. 2007, ApJ, 658, 778